

www.acsabm.org Article

Beyond Antiresorptive Activity: Risedronate-Based Coordination Complexes To Potentially Treat Osteolytic Metastases

Gabriel Quiñones Vélez, ^L Lesly Carmona-Sarabia, ^{Alexandra París Santiago,} Angélica F. Figueroa Guzmán, Chunhua Hu, Esther Peterson-Peguero, and Vilmalí López-Mejías*



Cite This: https://doi.org/10.1021/acsabm.2c00648



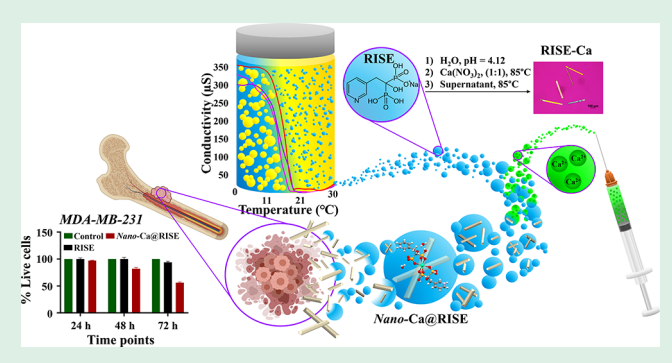
ACCESS I

III Metrics & More

Article Recommendations

s Supporting Information

ABSTRACT: Coordination of clinically employed bisphosphonate, risedronate (RISE), to bioactive metals, Ca²⁺, Mg²⁺, and Zn²⁺, allowed the formation of bisphosphonate-based coordination complexes (BPCCs). Three RISE-based BPCCs, RISE-Ca, RISE-Mg, and RISE-Zn, were produced, and their structures were elucidated by single crystal X-ray diffraction. Interestingly, the addition of an auxiliary ligand, etidronic acid (HEDP), resulted in the recrystallized protonated form of the ligand, H-RISE. The pH-dependent structural stability of the RISE-based BPCCs was measured by means of dissolution profiles under neutral and acidic simulated physiological conditions (PBS and FaSSGF, respectively). In comparison to RISE (*Actonel*), the complexes showed a



lower equilibrium solubility (~70–85% in 18–24 h) in PBS, while a higher equilibrium solubility (~100% in 3 h) in acidic media. The results point to the capacity to release this BP in a pH-dependent manner from the RISE-based BPCCs. Subsequently, the particle size of RISE-Ca was reduced, from 300 μm to ~350 d.nm, employing the phase inversion temperature (PIT)-nanoemulsion method, resulting in *nano*-Ca@RISE. Aggregation measurements of *nano*-Ca@RISE in 1% fetal bovine serum (FBS):H₂O was monitored after 24, 48, and 72 h to study the particle size longevity in physiological media, showing that the suspended material has the potential to maintain its particle size over time. Furthermore, binding assays were performed to determine the potential binding of *nano*-Ca@RISE to the bone, where results show higher binding (~1.7×) for the material to hydroxyapatite (HA, 30%) when compared to RISE (17%) in 1 d. The cytotoxicity effects of *nano*-Ca@RISE were compared to those of RISE against the human breast cancer MDA-MB-231 and normal osteoblast-like hFOB 1.19 cell lines by dose—response curves and relative cell viability assays in an *in vitro* setting. The results demonstrate that *nano*-Ca@RISE significantly decreases the viability of MDA-MB-231 with high specificity, at concentrations ~2–3× lower than the ones reported employing other third-generation BPs. This is supported by the fact that when normal osteoblast cells (hFOB 1.19), which are part of the tissue microenvironment at metastatic sites, were treated with *nano*-Ca@RISE no significant decrease in viability was observed. This study expands on the therapeutic potential of RISE beyond its antiresorptive activity through the design of BPCCs, specifically *nano*-Ca@RISE, that bind to the bone and degrade in a pH-dependent manner under acidic conditions.

KEYWORDS: bisphosphonates, risedronate, coordination complexes, binding, osteolytic metastases

■ INTRODUCTION

Every year in the United States, ~180 K patients are diagnosed with breast cancer, from which 30% are estimated to develop osteolytic metastases (OM). ^{1–3} Bisphosphonates (BPs), a class of drugs known as bone resorption inhibitors, ⁴ have been prescribed to treat and delay the progression of OM and other bone-related diseases. ^{1,2,5–8} BPs possess P–C–P bonds, which make them resistant to enzymatic hydrolysis by endogenous phosphatases. ^{1,8,9} Additionally, BPs present high affinity to the bone as they strongly bind to its main constituent, hydroxyapatite (HA). ^{1,2,10–13} BPs have mechanisms of action that allow them to affect cells other than osteoclasts, such as tumor cells that are prone to metastasize. ⁴ Multiple antitumor effects via indirect ($\gamma\delta$ T cells, angiogenesis) and direct

(tumor-cell apoptosis) mechanisms of BPs have been suggested through preclinical research.^{4,14} However, these findings remain unclear due to the relatively low bioavailability (<10%) of BPs, requiring high doses to provide the desired therapeutic effect.^{1,11-13,15,16}

First- and second-generation BPs (i.e., etidronate, clodronate, alendronate, pamidronate) present significantly lower

Received: July 21, 2022 Accepted: January 31, 2023



therapeutic potency compared to third-generation compounds of this class. ^{1,4} BPs belonging to this last group (i.e., risedronate, zoledronate) are characterized by the presence of a nitrogen-containing heterocyclic ring, which has been demonstrated to provide higher therapeutic efficacy against bone-related diseases. ⁴ Moreover, several studies have been conducted on zoledronate and suggest the potential of this third-generation BP for cancer therapy. ^{1,2,17–19} However, at the present there is insufficient evidence regarding the antitumor effects of risedronate (RISE, Figure 1) and

Figure 1. Molecular structure of RISE (*Actonel*, left), and acidic form of the pyridinyl BP (risedronic acid, right) employed for the design of RISE-based BPCCs.

undetermined possibilities of its therapeutic potential against OM and other metastatic cancers. This is because most of the drug undergoes renal clearance (87%), reaching a maximum absolute bioavailability of 0.62% (significantly low for a BP to kill cancer cells *in vitro*). ^{17,20}

RISE has been employed to design effective therapies against other diseases beyond its antiresorptive activity. This includes the design of coordination complexes as a novel approach for the treatment of *American trypanosomiasis* or Chagas disease, a parasitic disease. However, these studies are limited and do not focus on treating or preventing metastatic cancers.

In previous accounts, ^{22,23} BPs have been employed to design bisphosphonate-based coordination complexes (BPCCs), and assess their biomedical properties which might render them suitable as a potential therapy against OM. ^{22,23} Alendronate and zoledronate-based BPCCs have been previously reported. ^{22,23} These accounts describe the structure and biomedical properties of these materials and demonstrate that these possess pH-dependent degradation, high binding

affinity to the bone, low aggregation in biorelevant media, and cytotoxicity against MDA-MB-231 cells at low concentrations. ^{22,23} Other accounts have reported complexes where RISE coordinates with different metal ions such as Cd²⁺, Cu²⁺, Mg²⁺, Ni²⁺, Pb²⁺, and Zn^{2+,21,24,25} However, the focus of these reports is mainly on the structural properties of the materials and their applications for sensing, electronics, and therapies not related to bone diseases. ^{21,24,25}

Article

In this work, RISE coordinates with three different divalent metals $(M^{2+} = Ca^{2+}, Mg^{2+}, and Zn^{2+})$ to form RISE-based BPCCs (Figure 2). The selected metals are bioactive (LD₅₀ of 0.35, 1.0, and 8.1 g/kg, respectively) and promote osteoblastic bone formation and mineralization. 26-28 The solid-state and dissolution of these materials were characterized. Moreover, the phase inversion temperature (PIT)-nanoemulsion method was coupled to the synthesis to reduce the particle size of a selected RISE-based BPCC (RISE-Ca), thus resulting in the formation of nano-Ca@RISE. Additionally, several biomedical properties of nano-Ca@RISE were determined, which included its aggregation behavior, binding affinity, and cytotoxicity. This study intends to expand the therapeutic potential of RISE beyond its antiresorptive activity through the design of BPCCs, specifically nano-Ca@RISE, and provide initial evidence that can increase the interest in these as promising materials aimed at treating and preventing breast-cancer-induced OM.

■ EXPERIMENTAL SECTION

Materials. Calcium chloride dihydrate [CaCl₂·2H₂O, USP grade], calcium nitrate tetrahydrate [Ca(NO₃)₂·4H₂O, 99% pure], zinc chloride anhydrous [ZnCl₂, >98% pure], zinc nitrate hexahydrate [Zn(NO₃)₂·6H₂O, 98% pure], magnesium chloride anhydrous [MgCl₂, ≥98% pure], magnesium nitrate hexahydrate [Mg(NO₃)₂·6H₂O, 99% pure], and etidronic acid (HEDP) 60% aqueous solution were acquired from Sigma-Aldrich (St. Louis, MO). Monosodium risedronate hemipentahydrate (RISE, >97% pure) was purchased from TCI America (St. Portland, OR). For the pH adjustments, a stock solution of sodium hydroxide (NaOH, USP grade, 0.3 M) was employed. Nanopure water was used as a solvent in all syntheses. A complete list of materials employed for the dissolution, binding, aggregation, and cytotoxicity assays is provided in the Supporting Information.

Crystallization of H-RISE. Crystallization of H-RISE (protonated form) was carried out by preparing a ligand solution (RISE) in

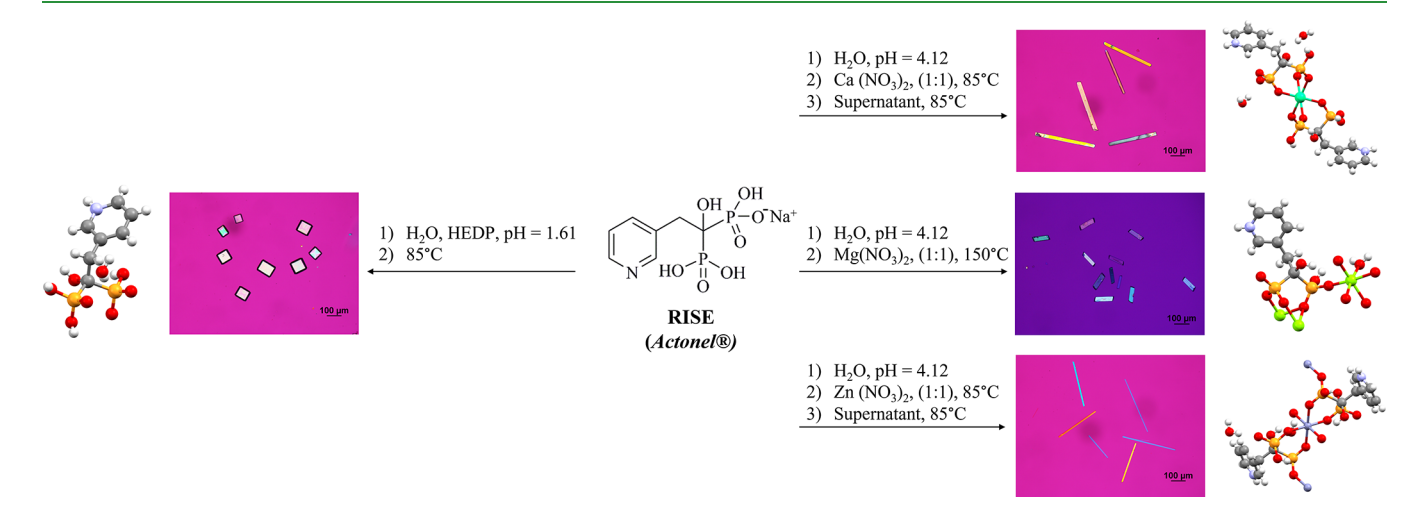


Figure 2. Schematic diagram of (right) the syntheses leading to three crystalline phases of RISE-based BPCCs, RISE-Ca, RISE-Mg, and RISE-Zn, and (left) crystallization of the protonated form of the ligand, H-RISE. The variables explored were M²⁺:RISE molar ratio, temperature, pH, metal salt anion (NO₃⁻ vs Cl⁻), and the addition of HEDP as an auxiliary ligand.

nanopure water. HEDP was added to adjust the pH (1.61) below the p K_a of RISE and to achieve complete protonation of the phosphonate groups. The solution was heated until solid particles were visible. The solid was collected by vacuum filtration and air-dried.

General Synthesis of RISE-Based BPCCs. Aqueous solutions of RISE and the respective metal salts were prepared separately. NaOH (0.3 M) was added dropwise to the ligand solution to adjust the pH (if needed) between 4.42 and 6.00. To prevent the formation of metal hydroxides, the pH adjustments were kept below the $M(OH)_n$ precipitation pH. The metal salt solution was added using a syringe to the ligand solution and mixed thoroughly. The resulting mixture was heated until solid particles were visible. Then it was removed from the heat source and left undisturbed to promote crystal growth. The solid was collected by vacuum filtration and air-dried. The nucleation induction times varied from minutes to hours. A detailed description of the synthesis of each of the BPCC (RISE-Ca, RISE-Mg, and RISE-Zn) is provided in the Supporting Information.

Raman Spectroscopy. A Thermo Scientific DXR Raman microscope was used to record all Raman spectra. The measurements were collected from 3,400 to $100~{\rm cm}^{-1}$ with a 532 nm laser a 400 lines/nm grating, and 50 $\mu{\rm m}$ slit by averaging 32 scans at 5 s exposures. The OMNIC for Dispersive Raman software v. 9.2.0 was employed for data analysis.

Scanning Electron Microscopy-Energy Dispersive Spectroscopy (SEM-EDS). SEM micrographs and XEDS spectra were collected using a JEOL JSM-6480LV SEM with an Evenhart Thomley secondary electron imaging (SEI) detector and an energy dispersive X-ray analysis (EDAX) Genesis 2000 detector. The samples used for SEM imaging were coated with a 5–10 nm layer of Au employing a PELCO SC-7 Auto Sputter Coater coupled with a PELCO FTM-2 Film Thickness Monitor for 10 s. SEM micrographs were taken with an electron beam of 11 mm width, and an acceleration voltage of 20 kV, and a spot size of 36, in high vacuum mode.

Powder X-ray Diffraction (PXRD). Diffraction patterns were collected in transmission mode using the Gandalfi mode from powder samples mounted using paratone oil on 0.3 mm Nylon loops. A Rigaku XtaLAB SuperNova X-ray diffractometer equipped with a microfocus Cu K α (λ = 1.5417 Å) radiation source operating at 50 kV and 0.8 mA and a HyPix3000 X-ray detector was used for data collection. Diffractogram patterns were integrated from 6° to 60° with a step size of 0.01° (Crystalliz PRO v. 1.171.3920a). The data collection was carried out at 100 K enabled by the use of an Oxford 800 Cryosystems Cryostream.

Single Crystal X-ray Diffraction (SCXRD). Crystals were observed under polarized light on a Nikon Eclipse microscope LV100NPOL, equipped with a Nikon DS-Fi2 camera (NIS Elements BR software v. 4.30.01). Suitable single crystals of H-RISE, RISE-Ca, RISE-Zn and RISE-Mg were mounted using paratone oil in MiTeGen micro loops.

The diffraction data for RISE-Mg was collected in a Bruker AXS SMART APEX-II equipped with a Mo K $_{\alpha}$ (λ = 0.71073 Å) radiation source operating at 50 kV and 40 mA, a monocap collimator, and APEX-II CCD detector. The data collection was carried out at 100 K enabled by the use of an Oxford 700 Cryosystems Cryostream. For H-RISE, RISE-Ca, and RISE-Zn, the diffraction data was collected in a Rigaku XtaLAB SuperNova single microfocus Cu Ka (λ = 1.5417 Å) radiation source operating at 50 kV and 0.8 mA equipped with a HyPix3000 X-ray detector (CrystallizPRO software v.1.171.3920a). The data collection was carried out at 100 K enabled by the use of an Oxford Cryosystems 800 Cryostream. The crystal structures of H-RISE, RISE-Ca, RISE-Zn, and RISE-Mg were solved by employing direct methods. The structure refinement was performed using full-matrix least-squares on F2 within the Olex2 software (v1.2). All non-hydrogen atoms were anisotropically refined.

Thermogravimetric Analysis (TGA). Powdered material (1–5 mg) was thermally treated from 10 to 700 °C at 5 °C/min (60 mL min $^{-1}$ of N₂ gas) using TGA Q500 (TA Instruments, Inc.). TA Universal Analysis software (v 4.3A) was employed for data analysis.

Dissolution Profiles. Dissolution profiles were recorded for the reagent grade RISE, H-RISE, RISE-Ca, RISE-Mg, and RISE-Zn in

PBS (pH = 7.40) and in fasted-state simulated gastric fluid (FaSSGF, pH = 1.60) by absorbance measurements (at $\lambda_{\rm max}$ = 260 nm) against a reagent blank using direct quantification. Dissolution assays were performed in 100 mL of PBS or FaSSGF buffers at 37 °C at 150 rpm for 48 h. Absorbance measurements were collected using a 400–200 nm scan on a Cary 100 Spectrophotometer (Agilent UV Cary Scan v.20.0.470). Further details of the quantification of RISE during dissolution measurements are provided in the Supporting Information.

Synthesis and Characterization of *nano***-Ca@RISE.** The phase inversion temperature (PIT) nano emulsion method was adapted to the synthesis of *nano*-Ca@RISE. ²³ Further details of the synthesis and characterization of *nano*-Ca@RISE as well as the aggregation measurements performed in 1% Fetal Bovine Serum (FBS):PBS are provided in the Supporting Information.

Binding Assay. The binding assay of *nano*-Ca@RISE was adapted from a previous publication.²³ Further details of the binding assay are provided in the Supporting Information.

Cell Culture. MDA-MB-231 triple-negative breast cancer cell line was grown in DMEM supplemented with 10% FBS and 1% Pen-Strep and incubated at 37 °C in 5% CO₂. Human fetal osteoblastic hFOB 1.19 cell line was grown in 1:1 DMEM:F12 supplemented with 10% FBS and 0.3 mg/mL G418 and incubated at 34 °C in 5% CO₂. Cells were passaged when they reach 80% confluency, and media was changed twice a week.

Cell Viability Studies. Briefly, 2.5×10^5 cell/mL cells were seeded in 96-well plates and incubated for 24 h at 37 °C (MDA-MB-231) and 34 °C (hFOB 1.19), respectively, to allow recovery and attachment of cells to the plate. Then cells were treated with 100 μ L per well of a 2-fold serial dilution of RISE (0-200 μ M), followed by incubation periods of 24, 48, and 72 h. The control groups for both cell lines were treated with the growth media described above. Cell viability was determined by incubating each cell line for 4 h with a final concentration of 10% AlamarBlue Viability reagent in PBS. Dose-response curves were generated to determine the half-maximal inhibitory concentration (IC₅₀) of the drug for each cell line. Fluorescent units were measured at $\lambda_{\rm exc}$ = 560 nm, $\lambda_{\rm em}$ = 590 nm in an Infinite M200 PRO Tecan Microplate Reader. The percentage of metabolic active cells (live cells) per treatment was calculated by comparing the viability of the cells treated with each concentration of RISE solutions to the control group representing 100% of live cells. Graph Pad Prism 8 was used to generate the dose-response curves (% cell live vs concentration) by using the nonlinear regression formula and to determine the IC₅₀.

After determining the IC $_{50}$ values for RISE, the percentage of Relative Cell Viability (%RCV) was determined with selected concentrations including the RISE IC $_{50}$ value (35, 40, 45, and 50 μ M) for both RISE and nano-Ca@RISE in both cell lines. Cell viability for each concentration was measured after 24, 48, and 72 h of treatment for both RISE and nano-Ca@RISE. Cell seeding and cell viability measurements were performed as described above. Graph Pad Prism 8 was utilized to plot the %RCV at each concentration per time point. All experiments were performed in triplicates, and statistical analysis was performed using mean, standard deviation, and the coefficient of variation percentage (%CV).

RESULTS AND DISCUSSION

Multiple conditions were explored varying the M²⁺:RISE molar ratio, temperature, pH, and anion, yielding only powdered or microcrystalline solids not suitable for structural elucidation by single crystal X-ray diffraction. Reported here are three crystalline phases obtained under almost identical conditions (Figure 2, right) except for the temperature. It was observed that the variation of the anion of the metal salt (NO₃⁻ vs Cl⁻) influences the crystal quality of the resulting RISE-based BPCCs. Employing the respective nitrate metal salt, three coordination complexes with good crystal quality for structural elucidation were obtained as shown in the polarized light

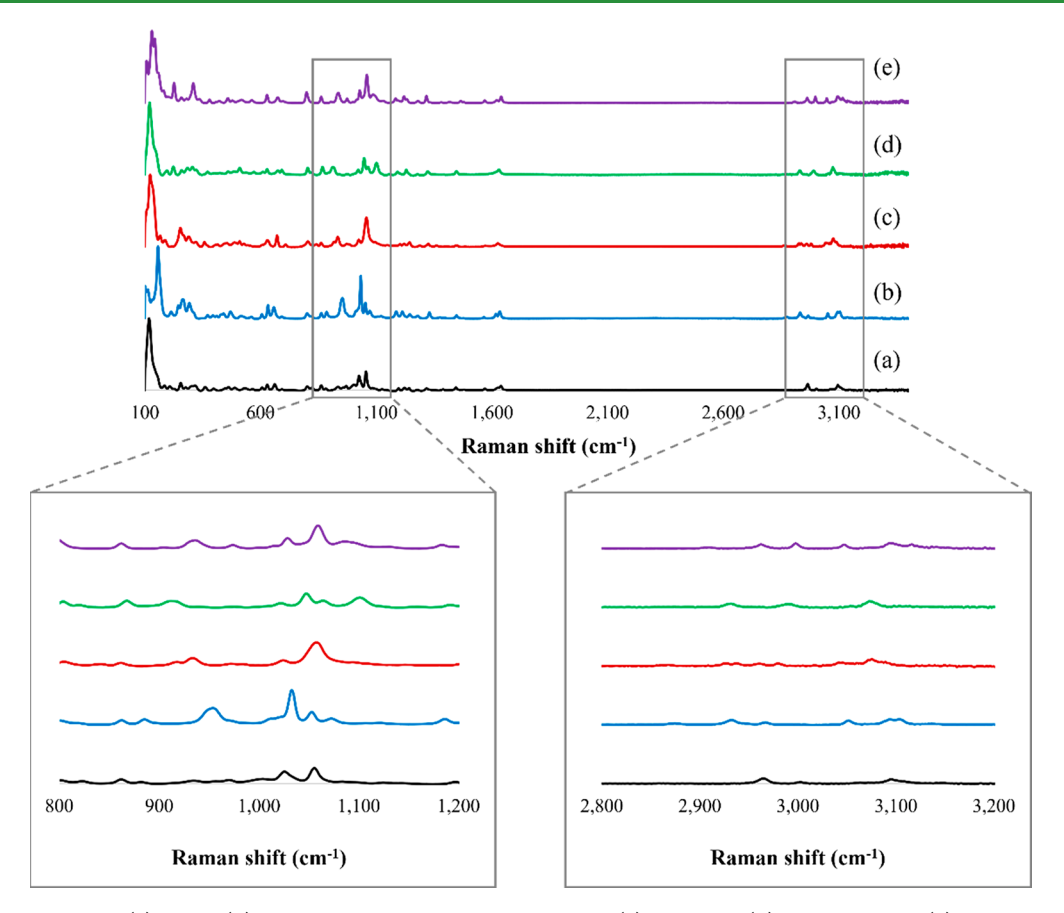


Figure 3. Raman spectra of (a) RISE, (b) H-RISE, and the RISE-based BPCCs (c) RISE-Ca, (d) RISE-Mg, and (e) RISE-Zn.

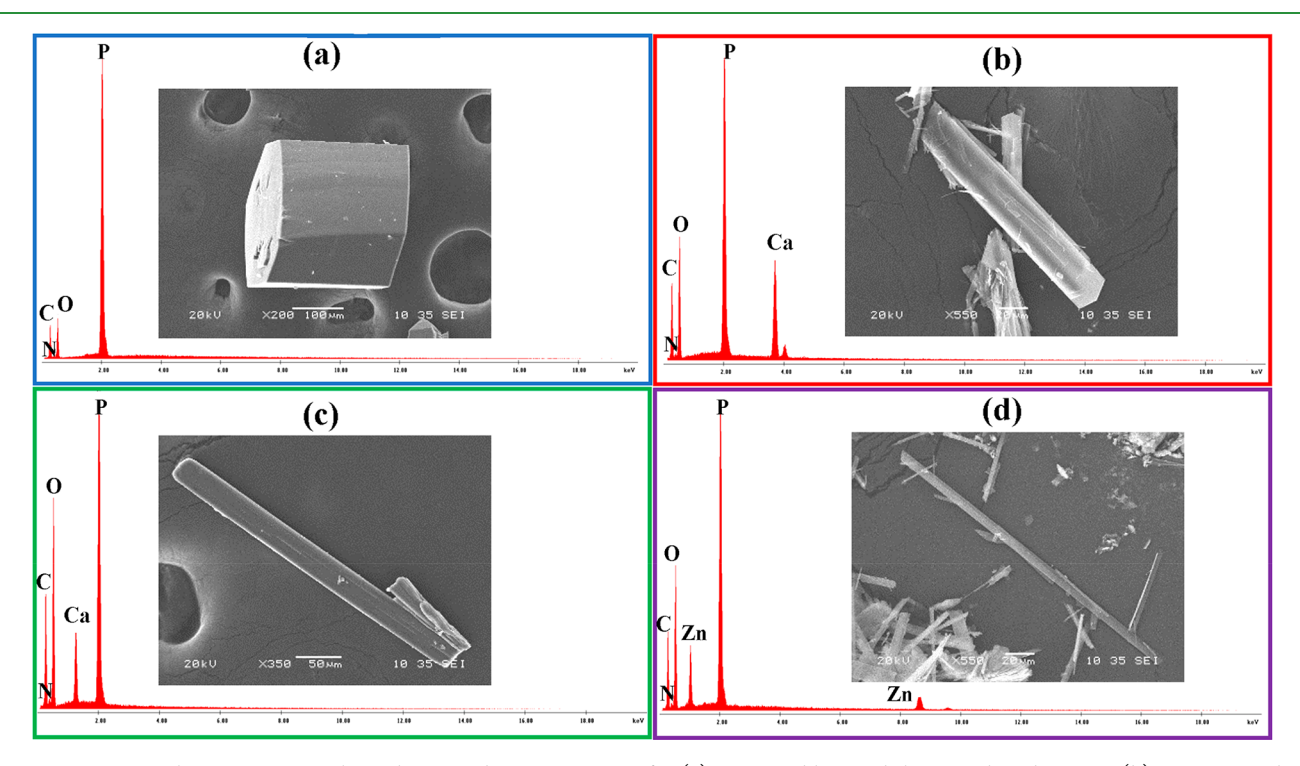


Figure 4. Scanning electron micrographs and energy dispersive spectra for (a) H-RISE, blue; and the RISE-based BPCCs (b) RISE-Ca, red; (c) RISE-Mg, green; and (d) RISE-Zn, purple.

micrographs (Figure 2). The reaction of RISE with the selected metal ions (Ca^{2+} , Mg^{2+} , and Zn^{2+}) produced crystals with a similar acicular habit (Figure 2). Interestingly, the

addition of HEDP as an auxiliary ligand significantly decreased the pH and yielded cubic crystals of RISE in its protonated form (H-RISE, Figure 2, left).

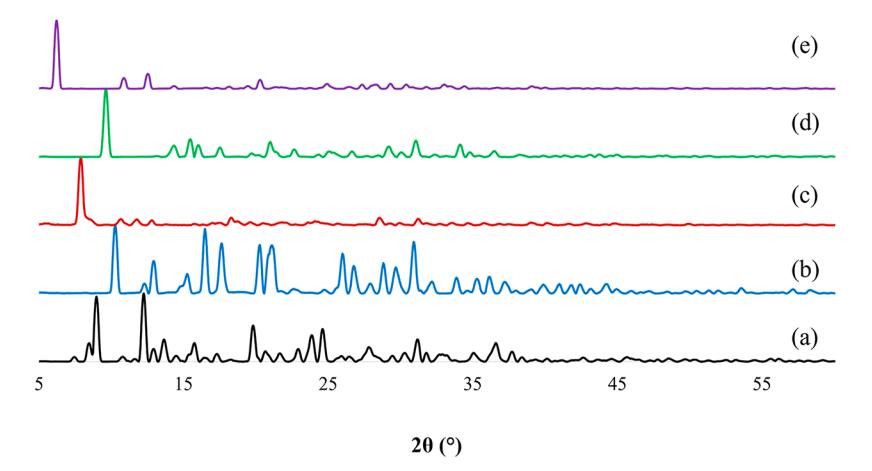


Figure 5. PXRD overlay of (a) RISE, (b) H-RISE, and the RISE-based BPCCs (c) RISE-Ca, (d) RISE-Mg, and (e) RISE-Zn.

■ RAMAN SPECTROSCOPY ANALYSIS

The Raman spectra of the RISE-based BPCCs are shown in Figure 3. The differences in Raman shift among H-RISE, RISE, and the RISE-based BPCCs confirmed that distinctive crystalline phases were produced. Characteristic bands corresponding to the hydrogen phosphate H-OPO₂C moieties (3,000-2,800 cm⁻¹) and the stretching vibrations $\nu O - H/H_2O$ (3,100-3,000 cm⁻¹) are unique to the RISEbased BPCCs (Figure 3, right zoom-in). These differences can be attributed to the coordination and hydrogen bonding between the coordinated and lattice waters present in these crystal structures. Compared to RISE, several Raman signals appear at \sim 3,000 and 3,100 cm $^{-1}$, which confirms the presence of strong hydrogen bonds and suggests that an extensive hydrogen bonding network is present in each of these crystal phases. H-RISE also presents additional signals around this region due to the presence of hydrogen bonds. The Raman signal at 1,320 cm⁻¹ can be assigned to the P=O deformation vibration, while the differences observed at ~1,190 cm⁻¹ are normally attributed to $\nu P = O/\delta^{\pi}POH$ stretching vibrations. The coordination sphere of the RISE-based PBCCs is confirmed by two bands occurring at ~1,100-1,060 cm⁻¹ and at ~1,020 cm⁻¹, respectively (Figure 3, left zoom-in). The former is a strong characteristic signal of the $\nu^{as}P-O(H)$ asymmetric stretching vibration, while the latter is a medium signal attributed to the δ PO-H bending. These signals are barely noticeable in the Raman spectra of RISE. However, for H-RISE, the signal corresponding to the δ PO-H bending is more intense due to the protonation of the phosphonate groups. The formation of a coordination sphere in the BPCCs is also supported by the absence of a strong signal at 960 cm⁻¹, which is present in H-RISE. This signal corresponds to the symmetric $\nu^{s}P-O(H)$ stretching vibrations of the protonated phosphonate groups of the ligand. This signal confirms the protonation of the phosphonate groups after H-RISE was crystallized. Due to the interaction of deprotonated phosphonate with the metal ions in the RISE-based BPCCs, the absence of a signal at this region was expected. Moreover, this symmetric stretching was expected to occur at lower Raman shifts (950-800 cm⁻¹) for the coordination complexes as observed in their Raman spectra. Vibrational modes are affected by changes in the P-O bond order as a result of the coordination bond. The differences in coordination between each BPCCs as well as the free ligand produce changes in the Raman spectra shown in both the symmetric and asymmetric

P-O(H) stretching vibrations. At a lower wavenumber (<1,000 cm $^{-1}$), other characteristic Raman shifts corresponding to the CH $_2$, C-C, C-P, C-OH, and M $^{2+}-$ O bonds can serve to distinguish each crystal phase.

MORPHOLOGICAL AND ELEMENTAL ANALYSIS

SEM micrographs show a distinct morphology for H-RISE and a similar but well-defined morphology for the RISE-based BPCCs (Figure 4). H-RISE crystallized in a cubic crystal habit, with crystal diameters between 200 and 300 μ m. The three RISE-based BPCCs crystallize in an acicular crystal habit, with needles that are 100-450 μ m long. Moreover, EDS spectra of the coordination complexes reveal characteristic signals for each of the elements present in the RISE-based BPCCs. This technique can identify the metal (calcium, magnesium, and zinc) employed in each synthesis as well as the elements (carbon, oxygen, nitrogen, and phosphorus) present in the RISE molecule (Figure 4). EDS spectra of H-RISE confirmed that the crystallized product was the BP ligand, the elemental signal for the metal was not observed in this sample. Collectively, the elemental and Raman analysis of the RISEbased BPCCs supports that three distinctive crystalline phases have been produced.

■ POWDER X-ray DIFFRACTION ANALYSIS (PXRD)

Figure 5 shows the powder diffractograms of RISE, H-RISE, and the coordination complexes. This technique reveals that these materials possess a high degree of crystallinity. Moreover, all three RISE-based BPCCs present unique diffractograms indicating that all phases are structurally distinct from one another. When compared to the starting materials, these observations confirm that the recrystallization of the ligand and the metal salt did not occur. The high angle peaks ($>5^{\circ}$ in 2θ) suggest that all phases are composed of 2D layers instead of 3D porous networks.

Other accounts have reported complexes where RISE coordinates with different metal ions. The diffraction patterns of these were compared to the ones described within this work (Supporting Information). Interestingly, the RISE-based BPCCs appear to be new phases when compared to the reported phases containing Cd²⁺, Cu²⁺, and Ni²⁺. 21,24,29

Table 1. Summary of the Crystallographic Parameters of H-RISE, RISE-Ca, RISE-Mg, and RISE-Zn^a

Compound	H-RISE	RISE-Ca	RISE-Mg	RISE-Zn
Empirical formula	$C_7H_{11}NO_7P_2\cdot H_2O$	$[Ca_{0.5}(C_7H_9NO_7P_2)]\cdot 2H_2O$	$[Mg(C_7H_9NO_7P_2)(H_2O)]$	$[Zn_{0.5}(C_7H_9NO_7P_2)]\cdot 2H_2O$
FW (g/mol)	301.12	338.17	323.42	349.81
Space group	$P2_1/n$	$P2_1/n$	$P2_1/n$	$P2_1/n$
Temperature (K)	104(5)	100.02(18)	100(2)	100(1)
λ (Å)	1.54184	1.54184	0.71073	1.54184
a (Å)	7.10270(10)	5.08867(5)	6.5076(7)	8.152(3)
b (Å)	10.69540(10)	16.59739(14)	12.4638(13)	28.2673(14)
c (Å)	14.7084(2)	15.19404(11)	13.6321(15)	10.101(3)
α (deg)	90	90	90	90
β (deg)	102.2280(10)	95.0417(8)	97.857(3)	149.02(8)
γ (deg)	90	90	90	90
$V(Å^3)$	1091.99(2)	1278.302(19)	1095.3(2)	1198.0(15)
Z	4	4	4	4
Z'	1	0.5	1	0.5
$ ho_{ m calc}~({ m g/cm^3})$	1.832	1.757	1.961	1.939
$R_{ m wp}$	0.1295	0.0735	0.1017	0.1723
$R_{ m p}$	0.0504	0.0271	0.0548	0.0620

^aAbbreviations: λ (X-ray source wavelength, Å), a/b/c (unit cell lengths, Å), $\alpha/\beta/\gamma$ (unit cell angle, deg), V (unit cell volume, ų), Z (number of formula units per unit cell), Z' (number of formula units per asymmetric unit), $\rho_{\rm calc}$ (unit cell calculated density, g/cm³), $R_{\rm wp}$ (weighted R-factor, %), and $R_{\rm p}$ (R-factor, %).

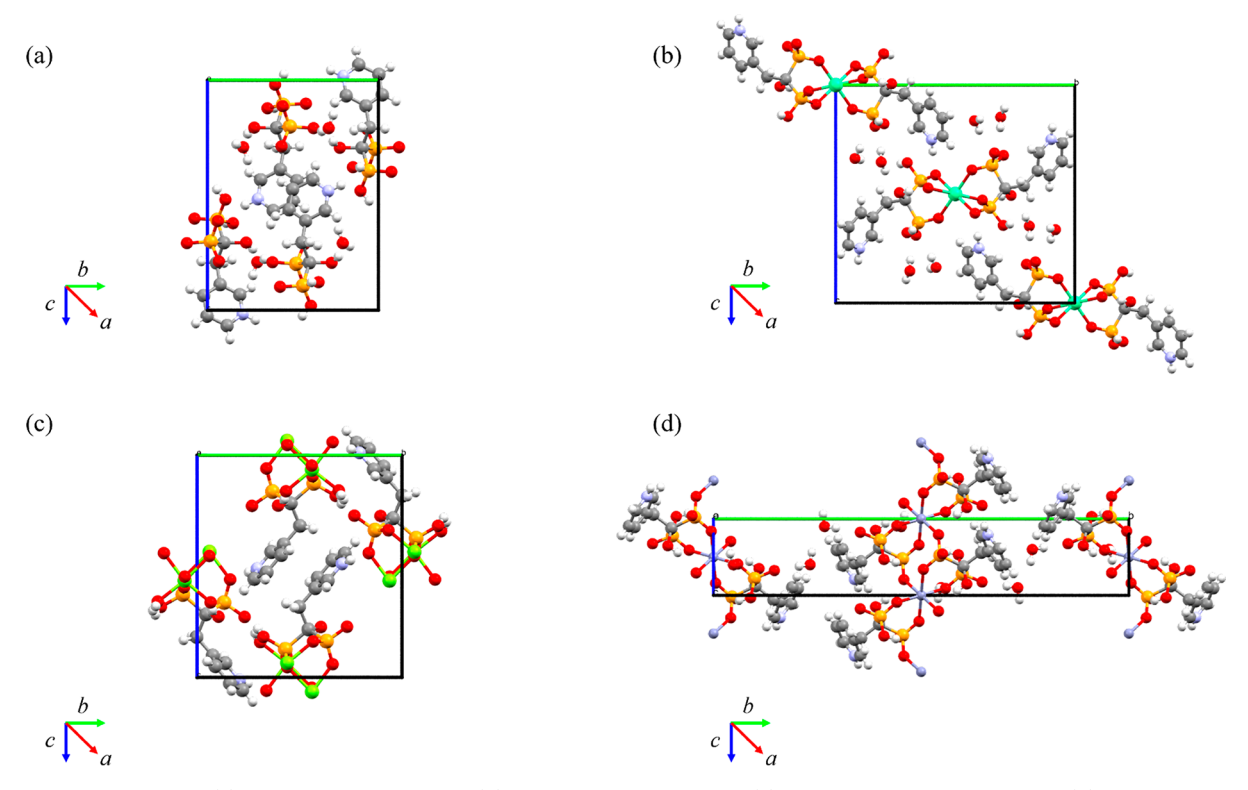


Figure 6. Packing motifs of (a) H-RISE along the a-axis, (b) RISE-Ca along the a-axis, (c) RISE-Mg along the a-axis, and (d) RISE-Zn along the a-axis.

SINGLE CRYSTAL X-ray DIFFRACTION (SCXRD) ANALYSIS

Structural elucidation of the three RISE-based BPCCs was performed to gain a better understanding of the structural motifs observed in this class of materials. Crystallographic parameters of the structure refinements for H-RISE and RISE-based BPCCs are summarized in Table 1, and their packing motifs are displayed in Figure 6. Additionally, Oak Ridge Thermal Ellipsoid Plots (ORTEPs), packing motifs, asym-

metric units, and simulated powder pattern overlays are available in the Supporting Information. Crystallographic data were deposited in the Cambridge Crystallographic Data Center (CCDC) for H-RISE (2181565), RISE-Ca (2181566), RISE-Mg (2181567), and RISE-Zn (2181568).

Structural Description of H-RISE. The compound $C_7H_{11}NO_7P_2\cdot H_2O$ crystallizes in the space group $P2_1/n$, containing a protonated RISE molecule in the asymmetric unit with a single lattice water molecule (Figure 6a). Four RISE molecules are contained within the unit cell (Z = 4). The

ACS Applied Bio Materials

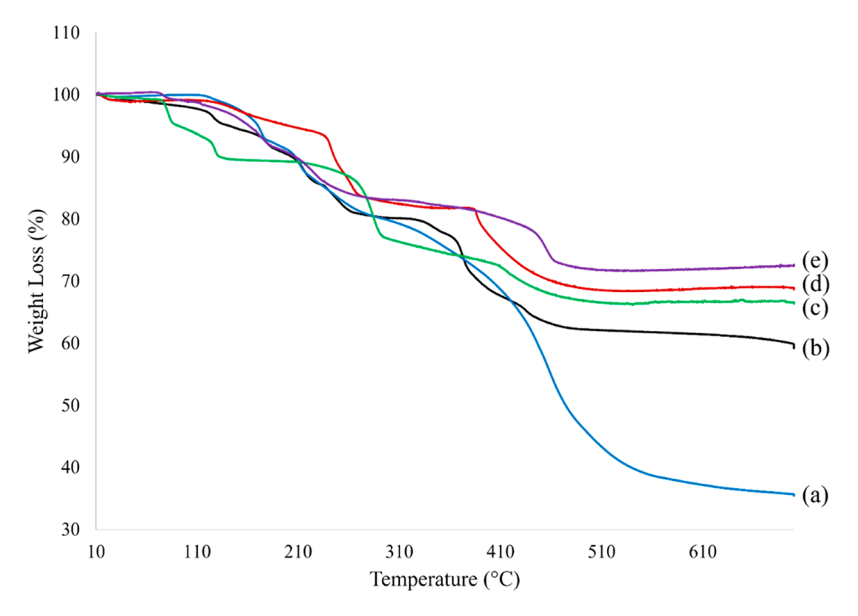


Figure 7. TGA thermographs of (a) H-RISE, (b) RISE, and the RISE-based BPCCs (c) RISE-Mg, (d) RISE-Ca, and (e) RISE-Zn.

conformation of the ligand is reinforced by a single intramolecular hydrogen bond between oxygens from the BP moieties (O2···O6, 3.026 Å). The RISE molecules are linked into molecular chains that propagate along the *a*-axis through strong intermolecular hydrogen bonds between the single lattice water molecule (O8···O1, 2.666 Å; O8···O5, 2.693 Å) and oxygen atoms from the BP group (O3···O6, 2.637 Å). Adjacent molecular chains are linked by intermolecular hydrogen bonds, resulting in their propagation along the *b*-axis (O4···O5, 2.717 Å; O7···O8, 2.489 Å). A single intermolecular hydrogen bond propagates molecular chains along the *c*-axis through the nitrogen of the pyridine and oxygen from the phosphonate moiety (N1···O6, 2.850 Å).

Structural Description of RISE-Ca. The structure of the compound [Ca_{0.5}(C₇H₉NO₇P₂)]·2H₂O, which crystallizes in the $P2_1/n$ space group, has not been previously reported (Figure 6b and Supporting Information). The asymmetric unit contains one bidentate RISE ligand coordinated to a Ca2+ center, surrounded by two uncoordinated water molecules. The Ca²⁺ center is in a distorted octahedral environment (supplementary angles: O1-Ca1-O3, 76.91°, O1-Ca1-O5, 82.42°, O3-Ca1-O5, 88.30°), with four coordinated ligands. Two unique binding modes are observed for the ligand. One RISE ligand is coordinated to the Ca²⁺ cation in a bidentate mode alternating oxygen from the BP, while another RISE ligand is in a monodentate mode. The Ca-O bond distances range between 2.263 and 2.367 Å. The metal cluster is linked by a single RISE molecule coordinated to form a chain (Ca1-O1-P1-O3-Ca1) that propagates slightly tilted along the aaxis. This chain is additionally reinforced by intermolecular hydrogen bonds (O3···O1, 2.571, and 2.935 Å; O6···O7, 2.766 Å). Adjacent molecular chains are linked by uncoordinated water that form hydrogen bonds either with the oxygens of the BP or water molecules along the b-axis (O2···O8, 2.637 Å, and O9···O8, 2.990 Å). The structure is reinforced by additional intramolecular hydrogen bonds through the b-axis, which involves the oxygens from the BP groups (O1···O2, 2.443 Å; O5···O6, 2.522; O5···O7, 2.570 Å). An extensive hydrogen bond network is facilitated by the uncoordinated water and the nitrogen from the pyridine group of the ligand, and these propagate adjacent molecular chains along the c-axis (O7...O9,

2.961 Å; O8···O7, 2.876 Å; O6···O8, 2.854 Å; N1···O1, 2.791 Å).

Structural Description of RISE-Mg. The compound $[Mg(C_7H_9NO_7P_2)(H_2O)]$ crystallizes in the $P2_1/n$ space group and represents a novel crystalline phase when compared to the RISE-based metal complexes that have been reported (Figure 6c and Supporting Information). The asymmetric unit has one RISE molecule coordinated to a Mg²⁺ center. The Mg2+ center is in a rather regular octahedral environment (supplementary angles: O1-Mg1-O5, 93.03°, O3-Mg1-O5, $85.14^{\circ},\,O1\text{--Mg1--O3},\,96.62^{\circ}),$ with three RISE ligands and a coordinated water molecule. The RISE ligand coordinates the metal center in a bidentate mode (O3-Mg1-O5 and O3-Mg1-O4) forming a six-membered chelate ring. The Mg-O bond distances range between 1.966 and 2.127 Å. The same ligand coordinates to the metal in a monodentate mode (Mg1-O1). Coordination between the Mg2+ cation and the O1 and O3 from the RISE molecule results in the formation of an eight-membered chelate ring that fuses adjacent metal centers, forming a chain that propagates through the a-axis. This chain is reinforced by intramolecular hydrogen bonds (O1···O3, 2.563 Å; O1···O5, 2.940 Å; O3···O4, 2.928 Å; O3··· O3, 2.927 Å). These chains propagate along the c-axis through an extensive hydrogen bond network in which the coordinated water molecules also participate (O6···O8, 2.968 Å; O6···O2, 2.480 Å). Propagation of the metal cluster through the *b*-axis can be described by intermolecular hydrogen bonds that form through the pyridine group of the ligand (O4···N2, 2.627 Å).

Structural Description of RISE-Zn. The compound $[Zn_{0.5}(C_7H_9NO_7P_2)]\cdot 2H_2O$ crystallizes in the space group $P2_1/n$, with one ligand coordinated to a Zn^{2+} center surrounded by two uncoordinated waters in the asymmetric unit (Figure 6d). The Zn^{2+} center is in a rather regular octahedral environment (*supplementary angles*: O1-Zn1-O2, 89.39° , O1-Zn1-O4, 91.47° , O2-Zn1-O4, 89.10°), with four RISE ligands coordinated. The Zn-O bond distances range from 2.010 to 2.166 Å. Intramolecular hydrogen bonds reinforce the metal cluster ($O2\cdots H7A-O7$, 2.648 Å). The BP ligand is coordinated to the metal center in a bidentate mode (O1-Zn1-O4), forming a six-membered chelate ring. The same ligand is coordinated to the Zn^{2+} center in a

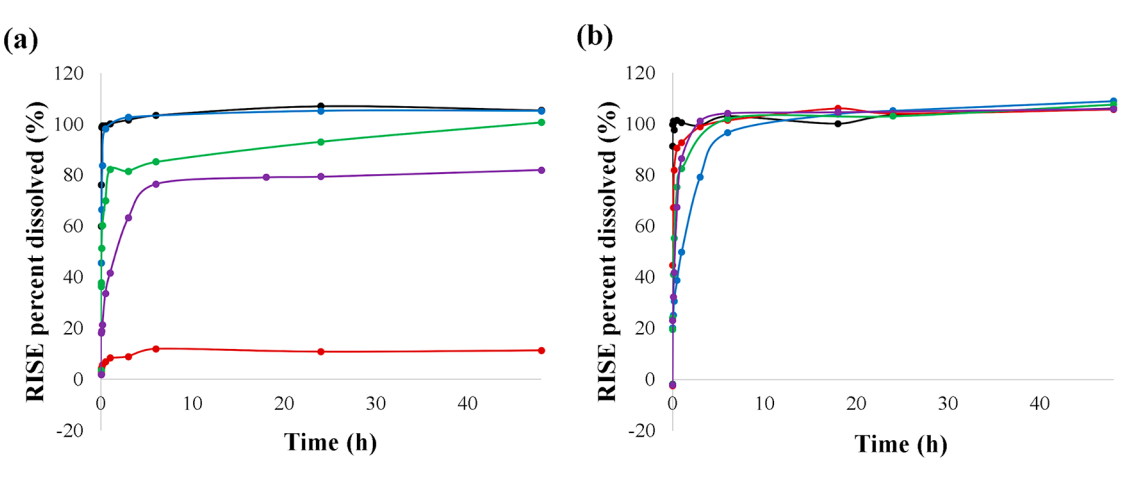


Figure 8. Complete dissolution profile of RISE (black), H-RISE (blue), RISE-Ca (red), RISE-Mg (green), and RISE-Zn (purple) in (a) PBS and (b) FaSSGF for 48 h.

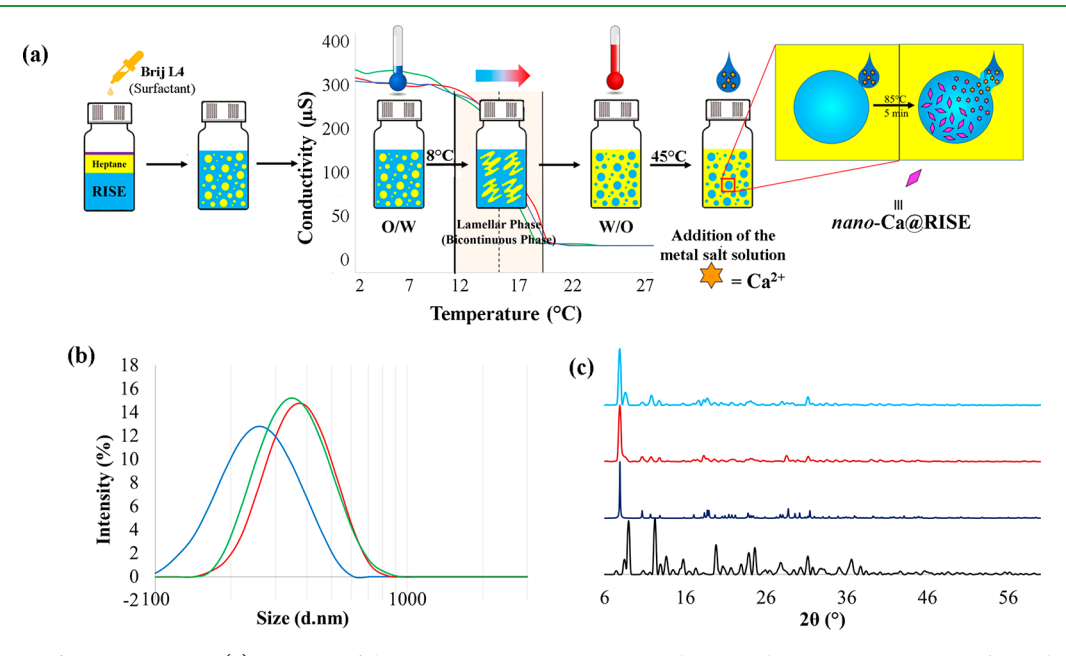


Figure 9. Synthesis of nano-Ca@RISE. (a) Diagram of the nano-Ca@RISE PIT nanoemulsion synthesis. PIT starts at \sim 11 °C and ends at \sim 20 °C, with a resulting inversion of phases at \sim 16 °C (dashed line). (b) Dynamic Light Scattering (DLS) spectra of the resulting crystals show an average particle size distribution of \sim 350 d.nm. (c) PXRD of RISE (black), RISE-Ca simulated powder pattern (navy blue), bulk RISE-Ca (red), and agglomerated nano-Ca@RISE (light blue).

monodentate mode (Zn1–O2). Coordination between the Zn²+ cation and the O1 and O2 from the RISE molecule results in the formation of an eight-membered chelate ring that fuses adjacent metal centers, resulting in the propagation of molecular chains through the *c*-axis. An extensive hydrogen bond network reinforces the chains along the *b*-axis connecting adjacent chains through one of the uncoordinated lattice waters (O6···O9, 2.774 Å; O9···O9, 2.792 Å). These chains propagate along the *a*-axis through an extensive hydrogen bond network that forms with either the pyridine group or the other uncoordinated water molecule (N1···O6, 2.683 Å; N1···O5, 3.026 Å; O3···O8, 2.642 Å; O8···O4, 2.775 Å; O8···O8, 2.969 Å). When compared to other structures of RISE-based coordination complexes previously reported, RISE-Zn also presents a unique packing arrangement.

■ THERMOGRAVIMETRIC ANALYSIS (TGA)

Three principal thermal events are observed in the TGA thermographs of the RISE-based BPCCs (Figure 7). These materials are stable up to 200 °C, where the first thermal event occurs, corresponding to the desolvation of uncoordinated lattice waters or coordinated water molecules. The organic combustion of the BP ligand is observed between 250 and 300 °C for each coordination complex. Lastly, at high temperatures, the thermal decomposition of the coordinated metal occurs. The third thermal event accounts for the minor weight loss observed at >400 °C.

TGA thermographs of the RISE-based BPCCs were compared to the ligand (RISE) and its protonated form (H-RISE). Results in Figure 7 showed that all RISE-based BPCCs possess higher thermal stability when compared to the RISE ligand (both the salt and protonated form). Higher thermal stability was observed for RISE-Ca when compared to RISE-Mg and RISE-Zn.

DISSOLUTION PROFILES FOR THE RISE-BASED BPCCs

The dissolution of RISE, H-RISE, and the RISE-based BPCCs in PBS (pH = 7.40) was assessed to verify the structural stability of these materials under neutral pH. The degradation of the RISE-based BPPCs was quantified via direct absorption measurements ($\lambda_{\rm max}$ = 260 nm). Dissolutions profiles of the RISE-based BPCCs were compared to that of RISE and H-RISE. The commercial dosage in RISE tablets is 35 mg, ^{30,31} and this corresponds to the total amount employed to obtain the dissolution profile of RISE-based BPCCs, H-RISE, and RISE (*Actonel*). The results from the dissolution profile in PBS (Figure 8a) demonstrate that RISE and H-RISE reached higher equilibrium solubility (100% in 30 min) than the RISE-based BPCCs (70–85% in 18–24 h). RISE-Ca reached a maximum concentration of RISE (10%) in 6 h, resulting in a lower equilibrium solubility in PBS.

To determine if the RISE-based BPCCs present a pHdependent degradation, the dissolution of the coordination complexes in FaSSGF (pH = 1.60) was performed. Results demonstrate that RISE (Actonel) presents a higher dissolution in FaSSGF than in PBS, reaching a maximum equilibrium solubility (100%) in 1 min (Figure 8b). Under these conditions, all RISE-based BPCCs presented significantly higher dissolution and equilibrium solubility (100% in 3 h), compared to their dissolution in PBS (70-85% in 18-24 h). The lowest dissolution observed corresponds to H-RISE, which reached a maximum equilibrium solubility (100%) in 18 h. The observed pH-dependent dissolution is desirable because it may allow RISE-based BPCCs to circulate longer and reach the target site while maintaining higher blood plasma concentrations for RISE. Once there, the increased acidic microenvironment at the metastatic site might enable the material to degrade and release the drug from the coordination complex.^{32–34} These results support the structural stability of the RISE-based BPCCs in simulated physiological media (PBS) and their ability to degrade in a pH-dependent manner under acidic conditions (FaSSGF), thus, controlling the release of the drug (RISE) from the coordination complex.

PHASE INVERSION TEMPERATURE (PIT)-NANOEMULSION SYNTHESIS OF nano-Ca@RISE

The PIT-nanoemulsion method was coupled to the synthesis of RISE-Ca to reduce its particle size (Figure 9a). RISE-Ca was selected because it presented higher thermal stability and a more drastic pH-dependent degradation than the other BPCCs. To determine the PIT temperature, conductivity measurements of a homogenized aqueous solution containing RISE, heptane, and a surfactant (BrijL4) were performed. The starting point is an oil-in-water (O/W) microemulsion, with an average conductivity of $\sim 340.0~\mu S$ at 2 °C. As the temperature is raised at 1 °C/min, a phase inversion occurs resulting in a water-in-oil (W/O) nanoemulsion with an average conductivity value of $\sim 9.74~\mu S$. For this system, the phase inversion started at 11 °C and ended at 20 °C making the average phase inversion temperature ~ 16 °C (Figure 9a).

After identifying the PIT, the hydrothermal synthesis for the RISE-Ca was adapted to the PIT-nanoemulsion method (Figure 9a) based on previous reports. Analysis of the resulting particles using dynamic light scattering (DLS) demonstrated average particle size distributions of 269.8,

ı

385.1, and 371.0 d.nm and an average polydispersity index (PDI) of 0.738, 0.604, and 0.495 (Figure 9b) for three independent syntheses. These PDI values are representative of moderately monodisperse particles. It is observed that by limiting the space available for the crystallization of RISE-Ca to occur, the particle size is decreased from \sim 300 μ m to \sim 350 d.nm, resulting in nano-Ca@RISE. To determine if the crystal phase of nano-Ca@RISE is representative of the bulk material (RISE-Ca), a micron-sized agglomerate of nano-Ca@RISE was analyzed by PXRD (Supporting Information). The results demonstrate that nano-Ca@RISE and RISE-Ca are isostructural (Figure 9c). Therefore, conditions employed in the PIT nanoemulsion method also provide control over the resulting crystal phase of nano-Ca@RISE.

AGGREGATION MEASUREMENTS OF nano-Ca@RISE

The aggregation of nano-Ca@RISE was monitored in simulated biological conditions (1% FBS:H₂O) after 24, 48, and 72 h. This analysis can provide evidence of the potential of this material to serve as a drug delivery system by assessing its ability to maintain a constant particle size (<500 nm) over time when suspended in media.³⁵ DLS results demonstrate a relatively homogeneous particle size distribution in the dispersant at every time point. Average particle size distribution values obtained for the three time points were 74.03 d.nm (24 h), 104.7 d.nm (48 h), and 112.0 d.nm (72 h, Figure 10). Furthermore, the PDI values for nano-Ca@RISE

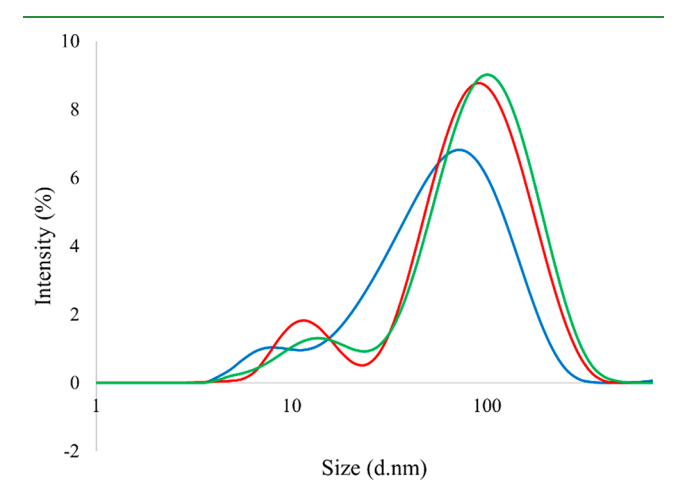


Figure 10. Particle size distribution of nano-Ca@RISE after 24 (blue), 48 (red), and 72 h (green) in 1% FBS:H₂O as determined by DLS.

particles were 0.578 (24 h), 0.479 (48 h), and 0.465 (72 h) which also support that nano-Ca@RISE does not significantly form larger aggregates over time while suspended in simulated biological conditions (1% FBS:H₂O).

■ BINDING ASSAYS OF nano-Ca@RISE TO HA

The capacity of *nano*-Ca@RISE to bind to HA, under simulated physiological conditions, was evaluated through a binding assay. The amount of *nano*-Ca@RISE bound to HA was quantified by monitoring the decrease in its concentration in the supernatant employing absorption measurements ($\lambda_{\text{max}} = 206 \text{ nm}$). Unlike previously investigated *nano*-BPCCs, ²³ the quantification of the binding was not measured by direct quantification using the wavelength of maximum absorption of the ligand (RISE, $\lambda_{\text{max}} = 260 \text{ nm}$). It was observed that the

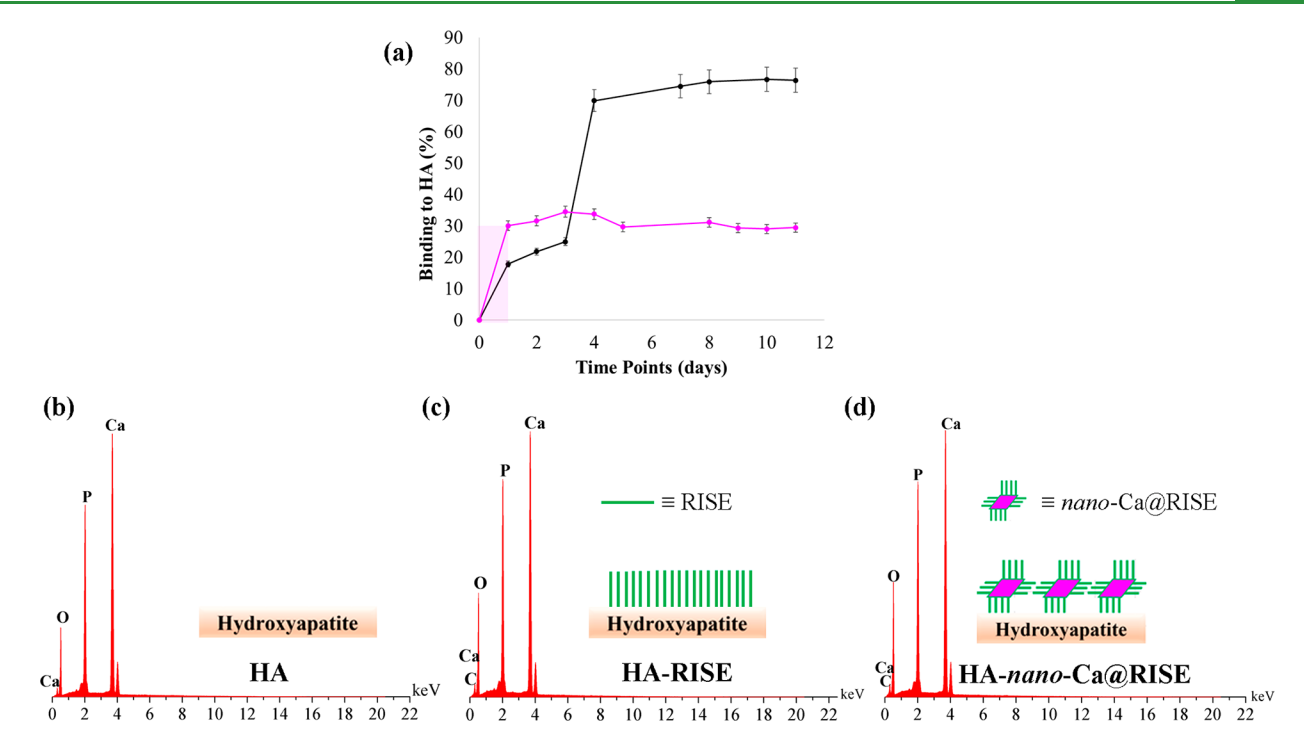


Figure 11. (a) Binding curves of RISE (control, black) and nano-Ca@RISE (experimental, pink) to HA in PBS, showing maximum binding of 76% (black dashed line) and 30% (pink dashed line), respectively. Duplicate measurements were performed. Error bars might not be visible if error falls below 5%. EDS spectra of (b) HA (control), (c) HA-RISE (control), and (d) HA-nano-Ca@RISE (experimental) after 48 h. A schematic is included in the EDS spectra for the proposed binding of these materials to HA.

RISE chromophore changes when coordinated with a divalent metal such as calcium (Ca^{2+}). The absorption spectrum of RISE compared to the one of *nano*-Ca@RISE revealed a shift in the wavelength of maximum absorption (λ_{max}) from 260 to 206 nm. This could be attributed to a quenching effect as the absorption of a substance decreases upon its coordination with a metal. Therefore, a new calibration curve for *nano*-Ca@RISE in PBS was employed to quantify *nano*-Ca@RISE in the supernatant after the binding assay (Supporting Information).

The binding curves (Figure 11a) show that 18% of RISE (control) binds to HA in 1 d and maximum binding (76%) occurs on day 8 when exposed to simulated physiological conditions (PBS, pH = 7.40). The results for nano-Ca@RISE show maximum binding (30%) is achieved in 1 d and sustained for 11 d under the same conditions. These assays support the higher binding (\sim 1.7×) for nano-Ca@RISE compared to the ligand within a relevant time point (Figure 11a, light pink region). It is presumed that the uncoordinated phosphate groups located at the crystal surface of nano-Ca@RISE enable its binding to HA (Supporting Information).

After the completion of the binding assays (48 h), an elemental analysis was performed to further demonstrate the binding of nano-Ca@RISE to HA (Figure 11b-d). A consequence of the binding to HA of both RISE ($C_7H_{10}NO_7P_2$, control) and nano-Ca@RISE [$Ca_{0.5}(C_7H_9NO_7P_2)\cdot 2H_2O$, experimental] was the significant differences in the relative composition of calcium and other charactertitc elemental signals on the EDS spectra (Table 2). For HA-RISE (38.63 wt %), the calcium weight percent decreased significantly when compared to HA (45.00 wt %). This can be attributed to the formation of a monolayer of RISE ($C_7H_{10}NO_7P_2$) on the surface of HA which would shield the detection of this element. For HA-nano-Ca@RISE, the relative weight percent of calcium (39.41 wt %) resulted in being

Table 2. Elemental Analysis Performed by EDS for HA (control), HA-RISE (control), and HA-nano-Ca@RISE (Experimental) after the Binding Assay^a

Element	HA ^b (wt %)	HA-RISE ^c (wt %)	HA-nano-Ca@RISE ^d (wt %)
Calcium	45.00	38.63	39.41
Carbon	_	3.93	6.43
Oxygen	36.36	39.25	37.54
Phosphorus	18.64	18.20	16.62

^aA magnification of 10,000× was used for all the surface measurements. ${}^{b}[Ca_{5}(OH)(PO_{4})_{3}].$ ${}^{c}(C_{7}H_{10}NO_{7}P_{2}).$ ${}^{d}[Ca_{0.5}(C_{7}H_{9}NO_{7}P_{2})]\cdot 2H_{2}O.$

higher than that for HA-RISE (38.63 wt %) but lower than that for HA (45.00 wt %). This result might be explained by the proposed binding of *nano*-Ca@RISE to HA, which suggests the formation of layers formed by particles on the HA surface. This would also shield the detection of the calcium signal by EDS. The difference in the relative concentration of calcium for HA-RISE and HA-*nano*-Ca@RISE is based on the absence of this metal in RISE (0 calcium per formula unit) versus its presence in *nano*-Ca@RISE (0.5 calcium per formula unit), which results in a slight increase of the detected calcium in the bound material.

■ CYTOTOXICITY ASSAYS OF nano-Ca@RISE

The effect of nano-Ca@RISE on cell viability was assessed and compared to RISE in two cell line models. The goal of this study is to determine the effectiveness and specificity of nano-Ca@RISE in affecting the viability of human breast cancer cell lines. Two in vitro models were employed, which include a human breast cancer (MDA-MB-231) cell line and a human fetal osteoblast (hFOB 1.19) cell line. The MDA-MB-231 is a

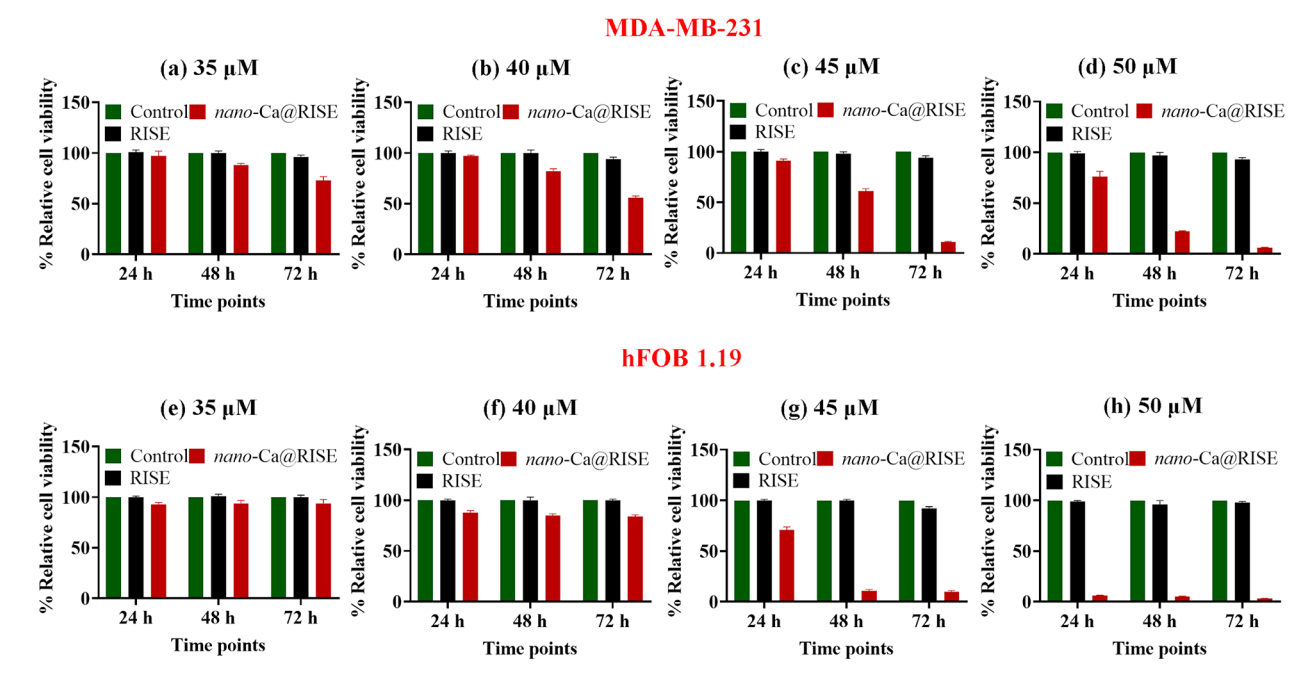


Figure 12. Percentage of relative cell viability (%RCV) for the human breast cancer MDA-MB-231 and normal osteoblast-like hFOB 1.19 cell lines, in green controls, RISE (black), and *nano*-Ca@RISE (red) at concentrations of (a, e) 35, (b, f) 40, (c, g) 45, and (d, h) 50 μ M after 24, 48, and 72 h of treatment.

triple-negative breast cancer cell line model of breast-cancerinduced OM, which also expresses micro-RNAs implicated in the process of breast cancer metastasis to the bone.^{3,36} hFOB 1.19 is an immortalized human fetal osteoblast cell line model used to study the differentiation of osteoblasts in vitro, and in this work it was used to represent the normal bone microenvironment. $^{37}~\rm IC_{50}$ values were calculated in both cell lines by treating them with RISE at concentrations of 0-200 µM. After treating the MDA-MB-231 cell line with RISE, an IC₅₀ value of 98 \pm 3 μ M was determined at 72 h, while for treatment at 48 h an IC₅₀ of 175 \pm 3 μM was observed. Moreover, at 24 h of treatment, an IC₅₀ > 200 μ M was obtained. This result demonstrated that RISE (0-200 μ M) significantly decreases the cell viability after 48 h of treatment against the MDA-MB-231 cell line. Moreover, the IC₅₀ for the hFOB 1.19 cell line was >200 μ M at the three time points, indicating that RISE $(0-200 \mu M)$ did not have a significant effect on cell viability after 72 h of treatment in these cells. The IC₅₀ curves for the above-described treatments can be found in the Supporting Information.

Furthermore, the %RCV was examined for both cell lines at concentrations of 35, 40, 45, and 50 μ M for RISE (control) and nano-Ca@RISE (experimental) during 24, 48, and 72 h. At a concentration of 35 μ M, the percentage of live cells was 73 \pm 3% for the MDA-MB-231 cell line when treated with nano-Ca@RISE after 72 h, as compared to RISE where the live cells were ~100% (Figure 12a). We can conclude that at a concentration of 35 µM the effect of nano-Ca@RISE on cell viability was relatively moderate. However, the decrease in cell viability for MDA-MB-231 treated with nano-Ca@RISE at 40 μ M was significantly higher with a %RCV of 82 \pm 3% and 56 ± 2%, after 48 and 72 h, respectively (Figure 12b). Interestingly, at 40 µM RISE still did not cause a decrease in cell viability (%RCV \approx 100%) against the MDA-MB-231. Moreover, a significantly higher cytotoxicity effect against the cancerous model was observed with nano-Ca@RISE treat-

ments at 45 and 50 µM. For treatment at 45 µM, a %RCV of 61 ± 2 and $11 \pm 1\%$ after 48 and 72 h, respectively, was observed for nano-Ca@RISE (Figure 12c). Thereafter, treating the cells with nano-Ca@RISE at 50 μM resulted in a drastic decrease in cell viability of MDA-MB-231 [%RCV, 22 ± 3 (48) h) and $6 \pm 1\%$ (72 h)], compared to the cells treated with RISE at this concentration [%RCV, 97 \pm 3 (48 h) and 93 \pm 2% (72 h), Figure 12d]. These results demonstrate that nano-Ca@RISE is more effective than RISE to induce cytotoxicity at concentrations ranging from 35 to 50 µM in an in vitro cell model of metastatic breast cancer to the bone. Noteworthy is the fact that nano-Ca@RISE was able to have a negative effect on cell viability in vitro against MDA-MB-231 cells at concentrations $\sim 2-3 \times$ lower than the ones reported employing other third-generation BPs, such as RISE and zoledronate.³⁸ In addition, compared to the commercial dosage of RISE (Actonel, 35 mg), the concentrations employed for the nano-Ca@RISE are outstandingly lower. 30,31

The cytotoxicity of nano-Ca@RISE was investigated in normal osteoblast-like cells and compared to that of RISE. The hFOB 1.19 cell line was treated with nano-Ca@RISE (experimental) and RISE (control), at the same concentrations used for the MDA-MB-231 assays. In this assay, after nano-Ca@RISE treatment, no significant cell growth inhibition against the hFOB 1.19 cell line (%RCV ≥ 80%, standard cell viability threshold) was expected, to prevent damage to the normal cell tissue at the bone microenvironment. 39,40 The cell viability results confirmed that no significant change in the percentage of live and metabolic active cells was observed after treatment with lower concentrations (35 and 40 μ M) of either RISE or nano-Ca@RISE after 24, 48, and 72 h. After treating the osteoblast-like cells with nano-Ca@RISE, the resulting % RCV values were $94 \pm 3\%$ (48 h) and $94 \pm 4\%$ (72 h) at 35 μ M (Figure 12e), while they were 85 \pm 2% (48 h) and 84 \pm 2% (72 h) at 40 μ M (Figure 12f). Moreover, at concentrations of 45 and 50 μ M, significant cytotoxicity effects were observed

against the hFOB 1.19 cell line after nano-Ca@RISE treatment, but not for RISE (%RCV \approx 100%). After 48 h of treatment with nano-Ca@RISE, %RCV values of 11 ± 1 (45 μ M) and 5 \pm 1% (50 μ M) were obtained, while, after 72 h, %RCV values of 10 ± 1 (45 μ M) and 3 \pm 1% (50 μ M) were observed (Figure 12g and 12h). These results show that at concentrations between 35 and 40 μ M nano-Ca@RISE has a more effective and specific effect on cytotoxicity against triplenegative breast cancer cells that metastasize to the bone (MDA-MB-231), without adversely affecting the viability of normal osteoblast cells (hFOB 1.19).

CONCLUSIONS

Herein, the reaction between clinically employed RISE and three biologically relevant metals (Ca²⁺, Mg²⁺, and Zn²⁺) resulted in three different crystal phases of RISE-based BPCCs. These BPCCs were characterized to gain a better understanding of the structural motifs observed in this class of materials. Based on the higher thermal stability and more drastic pH-dependent degradation under acidic conditions, RISE-Ca was selected for particle size reduction and for initial assessment of its biomedical properties. The crystal size of RISE-Ca (\sim 300 μ m) was significantly reduced by employing the PIT-nanoemulsion method, resulting in nano-Ca@RISE (~350 d.nm). More importantly, nano-Ca@RISE did not form larger aggregates when suspended in biologically relevant conditions (1% FBS:H₂O) after 24-72 h. These results suggest that nano-Ca@RISE could avoid excretion through phagocytosis mechanisms during cellular uptake as it meets particle size requirements. Furthermore, to investigate the ability of this material to bind to HA, and possibly provide localized therapeutic effects at the metastatic site, binding assays were performed. The results demonstrate that nano-Ca@RISE binds $\sim 1.7 \times$ more (30%) to HA than RISE (17%) in 1 d, suggesting that nano-Ca@RISE could bind to the main component of the bone at the metastatic site with higher affinity and within a relevant time frame. Subsequently, the cytotoxicity effects of nano-Ca@RISE were compared to that of RISE against the human breast cancer MDA-MB-231 and normal osteoblast-like hFOB 1.19 cell lines by dose-response curves and relative cell viability assays in an *in vitro* setting. The results of the cell viability study demonstrate that nano-Ca@ RISE significantly decreases the viability of MDA-MB-231 with high specificity, at concentrations $\sim 2-3 \times$ lower than the ones reported employing other third-generation BPs. This is supported by the fact that when normal osteoblast cells, which are part of the tissue microenvironment at metastatic sites, were treated with nano-Ca@RISE no significant decrease in viability was observed. Collectively, these results demonstrate that nano-Ca@RISE has the potential to treat cancerous cells that are prone to metastasize without significantly affecting a cell model that represents healthy tissue at the bone microenvironment. The properties exhibited by the RISE-based BPCCs regarding structure, dissolution, stability, binding, and cytotoxicity provide a strong support to further test the potential therapeutic benefit of these novel materials for a better management and/or prevention of breast-cancerinduced OM.

ASSOCIATED CONTENT

Supporting Information

The Supporting Information is available free of charge at https://pubs.acs.org/doi/10.1021/acsabm.2c00648.

Detailed experimental sections for the syntheses and characterization of the BPCCs including additional Raman spectra, PXRDs, SEM-EDS, TGAs, CIF files, ORTEPs, calibration curves, absorption spectra, dissolution profiles, DLS, binding curves, IC₅₀ curves and % RCV tables (PDF)

AUTHOR INFORMATION

Corresponding Author

Vilmalí López-Mejías — Department of Chemistry, University of Puerto Rico, San Juan, Puerto Rico 00931, United States; Crystallization Design Institute and the Molecular Sciences Research Center Inc., University of Puerto Rico, San Juan, Puerto Rico 00926, United States; orcid.org/0000-0003-2138-8414; Email: vilmali.lopez@upr.edu

Authors

Gabriel Quiñones Vélez — Department of Chemistry,
University of Puerto Rico, San Juan, Puerto Rico 00931,
United States; Crystallization Design Institute and the
Molecular Sciences Research Center Inc., University of Puerto
Rico, San Juan, Puerto Rico 00926, United States;
orcid.org/0000-0001-8789-1616

Lesly Carmona-Sarabia — Department of Chemistry, University of Puerto Rico, San Juan, Puerto Rico 00931, United States; Crystallization Design Institute and the Molecular Sciences Research Center Inc., University of Puerto Rico, San Juan, Puerto Rico 00926, United States

Alexandra París Santiago — Department of Chemistry, University of Puerto Rico, San Juan, Puerto Rico 00931, United States; Crystallization Design Institute and the Molecular Sciences Research Center Inc., University of Puerto Rico, San Juan, Puerto Rico 00926, United States; orcid.org/0000-0003-3488-3705

Angélica F. Figueroa Guzmán — Department of Chemistry, University of Puerto Rico, San Juan, Puerto Rico 00931, United States; Crystallization Design Institute and the Molecular Sciences Research Center Inc., University of Puerto Rico, San Juan, Puerto Rico 00926, United States; orcid.org/0000-0003-3486-3106

Chunhua Hu — Department of Chemistry and the Molecular Design Institute, New York University, New York, New York 10003-6688, United States; orcid.org/0000-0002-8172-2202

Esther Peterson-Peguero — Department of Biology, University of Puerto Rico, San Juan, Puerto Rico 00931, United States; orcid.org/0000-0001-7497-0980

Complete contact information is available at: https://pubs.acs.org/10.1021/acsabm.2c00648

Author Contributions

Gabriel Quiñones Vélez: Conceptualization, Data curation, Formal Analysis, Investigation, Methodology, Validation, Visualization, Writing-original draft, Writing-review and editing. Lesly Carmona-Sarabia: Conceptualization, Data curation, Formal Analysis, Investigation, Methodology, Validation, Visualization, Writing-original draft, Writing-review and editing. Alexandra París Santiago: Data curation, Formal Analysis, Investigation, Methodology, Writing-original draft, Writing-review and editing. Angélica Figueroa Guzmán: Data curation, Formal Analysis, Investigation, Methodology, Writing-original draft, Writing-review and editing. Tony Hu: Data

curation, Formal Analysis, Validation. Esther Peterson-Peguero: Formal Analysis, Validation, Writing-review and editing. Vilmali López-Mejias: Conceptualization, Funding acquisition, Investigation, Methodology, Project administration, Resources, Supervision, Validation, Visualization, Writing-review and editing.

Author Contributions

[⊥]G.Q.V. and L.C.-S. contributed equally.

Notes

The authors declare no competing financial interest.

ACKNOWLEDGMENTS

Gabriel Quiñones was initially supported by the National Institutes of Health-Research Initiative for Scientific Enhancement (NIH-RISE) Grant No. 5R25GM061151-15. Alexandra París and Angélica Figueroa were supported by the National Science Foundation-Research Experience for Undergraduates, Puerto Rico-Chemical Learning Integrated in Materials and Biomolecular Applications (NSF-REU CLIMB Program), under the Grant No. NSF-REU 1757365. Additionally, the authors gratefully acknowledge the Institutional Research Funds (FIPI Funds 2017-2019 and 2019-2021) of the University of Puerto Rico, Río Piedras Campus for financial support. The National Institutes of Health (1SC2GM127223-01A1), primarily funded the present work. The single crystal X-ray diffraction facilities at the University of Puerto Rico (CHE-1626103) and the New York University (CRIF/CHEM-0840277) were supported by grants from the National Science Foundation. The Puerto Rico Institute for Functional Nanomaterials (EPS-100241) Start-up Funds supported the acquisition of the TGA (TA Instruments, Inc.). Furthermore, we would like to express our gratitude to the personnel of the Materials Characterization Center (MCC) for their technical support during the acquisition of the SEM-EDS data.

REFERENCES

- (1) Lipton, A. Bisphosphonates and Metastatic Breast Carcinoma. *Cancer* **2003**, 97 (S3), 848–853.
- (2) Goldvaser, H.; Amir, E. Role of Bisphosphonates in Breast Cancer Therapy. *Curr. Treat. Options Oncol.* **2019**, 20 (4). DOI: 10.1007/s11864-019-0623-8.
- (3) Welsh, J. E. Animal Models for Studying Prevention and Treatment of Breast Cancer. In *Animal Models for the Study of Human Disease*; Elsevier Inc.: 2013; pp 997–1018. DOI: 10.1016/B978-0-12-415894-8.00040-3.
- (4) Roelofs, A. J.; Thompson, K.; Gordon, S.; Rogers, M. J.; Boyce; Roodman; Suva; Coleman; Weilbaecher; Bruland; Vesella; Lipton. Molecular Mechanisms of Action of Bisphosphonates: Current Status. Clin. Cancer Res. 2006, 12 (20), 6222s.
- (5) Hart, N. H.; Galvão, D. A.; Saunders, C.; Taaffe, D. R.; Feeney, K. T.; Spry, N. A.; Tsoi, D.; Martin, H.; Chee, R.; Clay, T.; Redfern, A.; Newton, R. Mechanical Suppression of Osteolytic Bone Metastases in Advanced Breast Cancer Patients: A Randomised Controlled Study Protocol Evaluating Safety, Feasibility and Preliminary Efficacy of Exercise as a Targeted Medicine. *Trials*. BioMed Central Ltd. December 20, 2018; pp 1–15. DOI: 10.1186/s13063-018-3091-8.
- (6) Diba, M.; Camargo, W. A.; Zinkevich, T.; Grünewald, A.; Detsch, R.; Kabiri, Y.; Kentgens, A. P. M.; Boccaccini, A. R.; Van Den Beucken, J. J. J. P.; Leeuwenburgh, S. C. G. Hybrid Particles Derived from Alendronate and Bioactive Glass for Treatment of Osteoporotic Bone Defects. J. Mater. Chem. B 2019, 7 (5), 796–808.

- (7) Mundy, G. R. Metastasis to Bone: Causes, Consequences and Therapeutic Opportunities. *Nature Reviews Cancer* **2002**, *2*, 584–593 August.
- (8) Paolino, D.; Licciardi, M.; Celia, C.; Giammona, G.; Fresta, M.; Cavallaro, G. Bisphosphonate-Polyaspartamide Conjugates as Bone Targeted Drug Delivery Systems. *J. Mater. Chem. B* **2015**, 3 (2), 250–259
- (9) Guenin, E.; Ledoux, D.; Oudar, O.; Lecouvey, M.; Kraemer, M. Structure-Activity Relationships of a New Class of Aromatic Bisphosphonates That Inhibit Tumor Cell Proliferation in Vitro. *Anticancer Res.* **2005**, 25 (2A), 1139–1145.
- (10) Giger, E. V.; Castagner, B.; Leroux, J. C. Biomedical Applications of Bisphosphonates. *J. Controlled Release* **2013**, *167* (2), 175–188.
- (11) Zeng, Y.; Sun, L.; Du, D.; He, X.; Shi, L. Lanthanide-Bisphosphonate Coordination Chemistry: Biocompatible Fluorescent Labeling Strategy for Hydrogel. ACS Appl. Bio Mater. 2021, 4, 1057.
- (12) Sun, B.; Gillard, M.; Wu, Y.; Wu, P.; Xu, Z. P.; Gu, W. Bisphosphonate Stabilized Calcium Phosphate Nanoparticles for E Ff Ective Delivery of Plasmid DNA to Macrophages. ACS Appl. Bio Mater. 2020, 3, 986.
- (13) Jing, C.; Li, B.; Tan, H.; Zhang, C.; Liang, H.; Na, H.; Chen, S.; Liu, C.; Zhao, L. Alendronate-Decorated Nanoparticles as Bone-Targeted Alendronate Carriers for Potential Osteoporosis Treatment. *ACS Appl. Bio Mater.* **2021**, *4*, 4907.
- (14) Clezardin, P.; Ebetino, F. H.; Fournier, P. G. Bisphosphonates and Cancer-Induced Bone Disease: Beyond Their Antiresorptive Activity. *J. Cancer Res.* **2005**, *65* (12), 4971–4974.
- (15) Lin, J. H. Bisphosphonates: A Review of Their Pharmacokinetic Properties. *Bone*; Elsevier Inc.; 1996; pp 75–85. DOI: 10.1016/8756-3282(95)00445-9.
- (16) Khosla, S.; Bilezikian, J. P.; Dempster, D. W.; Lewiecki, E. M.; Miller, P. D.; Neer, R. M.; Recker, R. R.; Shane, E.; Shoback, D.; Potts, J. T. Benefits and Risks of Bisphosphonate Therapy for Osteoporosis. *Journal of Clinical Endocrinology and Metabolism* **2012**, 97, 2272–2282.
- (17) Au, K. M.; Satterlee, A.; Min, Y.; Tian, X.; Kim, Y. S.; Caster, J. M.; Zhang, L.; Zhang, T.; Huang, L.; Wang, A. Z. Folate-Targeted PH-Responsive Calcium Zoledronate Nanoscale Metal-Organic Frameworks: Turning a Bone Antiresorptive Agent into an Anticancer Therapeutic. *Biomaterials* **2016**, 82 (2016), 178–193.
- (18) Li, W.; Xin, X.; Jing, S.; Zhang, X.; Chen, K.; Chen, D.; Hu, H. Organic Metal Complexes Based on Zoledronate-Calcium: A Potential PDNA Delivery System. *J. Mater. Chem. B* **2017**, *5* (8), 1601–1610.
- (19) Liu, D.; Kramer, S. A.; Huxford-phillips, R. C.; Wang, S.; Della Rocca, J.; Lin, W. Coercing Bisphosphonates to Kill Cancer Cells with Nanoscale Coordination Polymers. *Chem. Commun.* **2012**, *48*, 2668–2670.
- (20) Mitchell, D. Y.; Barr, W. H.; Eusebio, R. A.; Stevens, K. A. P.; Duke, F. P.; Russell, D. A.; Nesbitt, J. D.; Powell, J. H.; Thompson, G. A. Risedronate Pharmacokinetics and Intra- and Inter-Subject Variability upon Single-Dose Intravenous and Oral Administration. *Pharm. Res.* **2001**, *18* (2), 166–170.
- (21) Demoro, B.; Caruso, F.; Rossi, M.; Benítez, D.; Gonzalez, M.; Cerecetto, H.; Parajón-Costa, B.; Castiglioni, J.; Galizzi, M.; Docampo, R.; Otero, L.; Gambino, D. Risedronate Metal Complexes Potentially Active against Chagas Disease. *J. Inorg. Biochem.* **2010**, *104* (12), 1252–1258.
- (22) Quiñones Vélez, G.; Carmona-Sarabia, L.; Rodríguez-Silva, W. A.; Rivera Raíces, A. A.; Feliciano-Cruz, L.; Hu, C. T.; Peterson, E. A.; Lopez-Mejias, V. Potentiating Bisphosphonate-Based Coordination Complexes to Treat Osteolytic Metastases. *J. Mater. Chem. B* **2020**, 8 (10), 2155–2168.
- (23) Quiñones Vélez, G.; Carmona-Sarabia, L.; Rivera Raíces, A. A.; Hu, C. T.; Peterson-Peguero, E. A.; Lopez-Mejias, V. High affinity zoledronate-based metal complex nanocrystals to potentially treat osteolytic metastases. *Mater. Adv.* **2022**, *3*, 3251–3266.

- (24) Hu, J.; Zhao, J.; Hou, H.; Fan, Y. Syntheses, Structures and Fluorescence Studies of Two New Cadmium(II) Pyridyl-Diphosphonates. *Inorg. Chem. Commun.* **2008**, *11* (10), 1110–1112.
- (25) Bretti, C.; De Stefano, C.; Cardiano, P.; Cataldo, S.; Pettignano, A.; Arena, G.; Sgarlata, C.; Ida Grasso, G.; Lando, G.; Sammartano, S. Risedronate Complexes with Mg^{2+} , Zn^{2+} , Pb^{2+} , and Cu^{2+} : Species Thermodynamics and Sequestering Ability in NaCl at Different Ionic Strengths and at T=298.15 K. J. Mol. Liq. 2021, 343, 117699.
- (26) Kennel, K. A.; Drake, M. T. Adverse Effects of Bisphosphonates: Implications for Osteoporosis Management. *Mayo Clinic Proceedings*; Elsevier Ltd: 2009; pp 632–638. DOI: 10.4065/84.7.632.
- (27) Castiglioni, S.; Cazzaniga, A.; Albisetti, W.; Maier, J. A. M. Magnesium and Osteoporosis: Current State of Knowledge and Future Research Directions. *Nutrients*; MDPI AG: 2013; pp 3022–3033. DOI: 10.3390/nu5083022.
- (28) Yamaguchi, M. Role of Nutritional Zinc in the Prevention of Osteoporosis. *Mol. Cell. Biochem.* **2010**, 338, 241–254.
- (29) Barbey, C.; Lecouvey, M. Crystal Structure of (1-Hydroxy-1-Phosphono-2-Pyridin-3-Yl-Ethyl)-Phos-Phonic Acid (Risedronate), C7H11NO7P2 · H2O, an Antiresorptive Bones Drug. Zeitschrift fur Krist. New Cryst. Struct. 2002, 217 (JG), 137–138.
- (30) Walker, A. D.; Adachi, J. D. In Vitro Disintegration Studies of Weekly Generic and Branded Risedronate Sodium Formulations Available in Canada. *Curr. Med. Res. Opin.* **2011**, *27* (9), 1749–1754.
- (31) Reid, D. M.; Hosking, D.; Kendler, D.; Brandi, M. L.; Wark, J. D.; Marques-Neto, J. F.; Weryha, G.; Verbruggen, N.; Hustad, C. M.; Mahlis, E. M.; Melton, M. A Comparison of the Effect of Alendronate and Risedronate on Bone Mineral Density in Postmenopausal Women with Osteoporosis: 24-Month Results from FACTS-International. *Int. J. Clin. Pract.* 2008, 62 (4), 575–584.
- (32) Kato, Y.; Ozawa, S.; Miyamoto, C.; Maehata, Y.; Suzuki, A.; Maeda, T.; Baba, Y. Acidic Extracellular Microenvironment and Cancer. *Cancer Cell Int.* **2013**, *13* (1), 89.
- (33) Coleman, R.; Body, J. J.; Aapro, M.; Hadji, P.; Herrstedt, J. Bone Health in Cancer Patients: ESMO Clinical Practice Guidelines. *Ann. Oncol.* **2014**, 25, iii124–137.
- (34) Tsuzuki, S.; Park, S. H.; Eber, M. R.; Peters, C. M.; Shiozawa, Y. Skeletal Complications in Cancer Patients with Bone Metastases. *International Journal of Urology*. Blackwell Publishing; October 1, 2016; pp 825–832. DOI: 10.1111/iju.13170.
- (35) Pugazhendhi, A.; Edison, T. N. J. I.; Karuppusamy, I.; Kathirvel, B. Inorganic Nanoparticles: A Potential Cancer Therapy for Human Welfare. *International Journal of Pharmaceutics*; Elsevier B.V. March 25, 2018; pp 104–111. DOI: 10.1016/j.ijpharm.2018.01.034.
- (36) Croset, M.; Clézardin, P. MicroRNA-Mediated Regulation of Bone Metastasis Formation: From Primary Tumors to Skeleton. In *Bone Cancer: Primary Bone Cancers and Bone Metastases*, 2nd ed.; Elsevier Inc.: 2014; pp 479–489. DOI: 10.1016/B978-0-12-416721-6.00041-8.
- (37) Harris, S. A.; Enger, R. J.; Riggs, L. B.; Spelsberg, T. C. Development and Characterization of a Conditionally Immortalized Human Fetal Osteoblastic Cell Line. *J. Bone Miner. Res.* **1995**, *10* (2), 178–186.
- (38) Au, K. M.; Satterlee, A.; Min, Y.; Tian, X.; Kim, Y. S.; Caster, J. M.; Zhang, L.; Zhang, T.; Huang, L.; Wang, A. Z. Folate-Targeted PH-Responsive Calcium Zoledronate Nanoscale Metal-Organic Frameworks: Turning a Bone Antiresorptive Agent into an Anticancer Therapeutic. *Biomaterials* **2016**, *82*, 178–193.
- (39) Di Paolo, C.; Müller, Y.; Thalmann, B.; Hollert, H.; Seiler, T. B. P53 Induction and Cell Viability Modulation By Genotoxic Individual Chemicals and Mixtures. *Environ. Sci. Pollut. Res.* **2018**, 25 (5), 4012–4022.
- (40) Nwakiban, A. P. A.; Cicolari, S.; Piazza, S.; Gelmini, F.; Sangiovanni, E.; Martinelli, G.; Bossi, L.; Carpentier-Maguire, E.; Tchamgoue, A. D.; Agbor, G.; Kuiate, J.; Beretta, G.; Dell'Agli, M.; Magni, P. Oxidative Stress Modulation by Cameroonian Spice Extracts in HepG2 Cells: Involvement of Nrf2 and Improvement of Glucose Uptake. *Metabolites* **2020**, *10* (5), 182.